Optical and magnetic investigation of multiferroic and magnetocaloric properties of Nd0.8Tb0.2Mn2O5

S Mansouri, M Balli, S Jandl, A O Suleiman, P Fournier, M Orlita, I A Zobkalo, S N Barilo, M Chaker

Optical and magnetic investigation of multiferroic and magnetocaloric properties of $Nd_{0.8}Tb_{0.2}Mn_2O_5$

S. Mansouri,[1,*] M. Balli,[2] S. Jandl,[3] A. O. Suleiman,[1] P. Fournier,[3] M. Orlita,[4,5] I. A. Zobkalo,[6] S. N. Barilo,[7] and M. Chaker[1,†]

[1]*Centre Énergie, Matériaux et Télécommunications, Institut National de la Recherche Scientifique, 1650, Boulevard Lionel-Boulet, Varennes, Québec J3X 1P7, Canada*

[2]*AMEEC Team, LERMA, International University of Rabat, Parc Technopolis, Rocade Rabat-Salé 11100, Morocco*

[3]*Institut Quantique et Regroupement québécois sur les matériaux de pointe, Département de Physique, Université de Sherbrooke, Sherbrooke, J1K 2R1 Canada*

[4]*Laboratoire National des Champs Magnétiques Intenses, LNCMI-EMFL, CNRS UPR3228, Univ. Grenoble Alpes, Univ. Toulouse, INSA-T, Grenoble and Toulouse, France*

[5]*Institute of Physics, Charles University, Ke Karlovu 5, Prague 121 16, Czech Republic*

[6]*Petersburg Nuclear Physics Institute, NRC Kurchatov Institute, Orlova Roshcha, Gatchina, St. Petersburg district 188300, Russia*

[7]*Scientific-Practical Materials Research Centre NAS of Belarus, Minsk 220072, Belarus*

(Received 20 March 2022; revised 19 June 2022; accepted 22 July 2022; published 4 August 2022)

The multiferroic and the rotating magnetocaloric properties of $Nd_{0.8}Tb_{0.2}Mn_2O_5$ are investigated by microscopic optical probes and macroscopic magnetic measurements. Raman-active phonons as a function of temperature, and Nd^{3+} and Tb^{3+} infrared active crystal-field (CF) excitations as a function of temperature and under magnetic fields up to 11 T have been studied in $Nd_{0.8}Tb_{0.2}Mn_2O_5$. The obtained results are compared to those of $NdMn_2O_5$ and $TbMn_2O_5$ reference compounds. The observation of one set of Raman-active phonons and CF excitations rule out possible twinning while their energy positions and thermal evolutions indicate noticeable changes of Mn1-O3-Mn1 and TbO_8 structural units. This would explain the nature of separated magnetic phases in $Nd_{0.8}Tb_{0.2}Mn_2O_5$. The degeneracy of the ground-state Kramers doublet is lifted ($\Delta_0 \sim 9\,cm^{-1}$), indicating that the Nd^{3+}–Mn^{3+} interaction impacts the magnetic and ferroelectric properties of $Nd_{0.8}Tb_{0.2}Mn_2O_5$. The Zeeman splitting of excited crystal-field levels of the Nd^{3+} ions at low temperatures shows that the g_z factor is weak compared to that in $NdMn_2O_5$. This indicates that the R^{3+} spins in $Nd_{0.8}Tb_{0.2}Mn_2O_5$ are mostly aligned within the *ab*-plane. The nature of magnetocrystalline anisotropy in $Nd_{0.8}Tb_{0.2}Mn_2O_5$ as well as in all RMn_2O_5 compounds is quantitatively investigated by studying the anisotropy of paramagnetic Curie temperatures along ($\theta_{||}$) and perpendicular ($\theta_{\perp}$) to the *c* axis, ($\theta_{||} - \theta_{\perp}$), as a function of the rare-earth atomic number. It is particularly found that the magnetocrystalline anisotropy is mainly determined by the quadrupolar charge distribution of $4f$ shells. The rotating magnetocaloric effect in $Nd_{0.8}Tb_{0.2}Mn_2O_5$ is also evaluated and compared to that in $NdMn_2O_5$ and $TbMn_2O_5$. Our findings show that Nd- and Tb- separated magnetic phases independently contribute to the magnetocaloric effect of $Nd_{0.8}Tb_{0.2}Mn_2O_5$.

DOI: 10.1103/PhysRevB.106.085107

I. INTRODUCTION

RMn_2O_5, where R is rare-earth atom, are prototype materials of multiferroics of type II where the ferroic order is induced or enhanced by a particular spin arrangement that breaks the inversion symmetry [1–3]. These multiferroic materials have attracted great attention as they are candidates for the next generation of data storage devices and cryomagnetocaloric refrigeration such as the liquefaction of hydrogen/helium gases [4–9]. Indeed, a giant rotating magnetocaloric effect (RMCE) at relatively low magnetic fields was recently reported in $TbMn_2O_5$ and $HoMn_2O_5$ single crystals, opening a new perspective for the implementation of compact, simplified, and efficient magnetic refrigerators working at low temperatures [7,8]. This giant RMCE is mainly attributed to the strong magnetocrystalline anisotropy shown by these crystals [7–9]. In this way, the control of such a RMCE requires therefore an understanding of the origin of magnetocrystalline anisotropy in the fascinating family of RMn_2O_5 multiferroics. The strong magnetoelectric effect of RMn_2O_5 compounds is associated with unusual commensurate-incommensurate magnetic transitions where the magnetism of rare earth seems to play a key role [10–14]. Their spontaneous electric polarization, along their *b* axis, can reach values as large as $P_{//b} > 3000\,\mu C\ m^{-2}$ [10]. This magnetoelectric coupling depends strongly on the size of rare-earth elements [10–13]. Accordingly, the RMn_2O_5 compounds with large ionic radii (R = La and Pr) are classified as paraelectrics due to the absence of detectable electric polarization [13]. In contrast, those with small ionic radii (R = Sm to Lu) exhibit a finite

*sabeur.mansouri@inrs.ca
†chaker@inrs.ca

electric polarization [11]. The $NdMn_2O_5$ compound is the intermediate-size member of this family. It represents a particular case between the nonferroelectric $PrMn_2O_5$ and the ferroelectric $SmMn_2O_5$. It is considered as a weak ferroelectric with a spontaneous electric polarization of $\sim 2.4\,\mu C\ m^{-2}$, two orders of magnitude lower than that of other multiferroic members of RMn_2O_5 family [14]. Furthermore, its electrical polarization develops at $T_2 \sim 26 \pm 2$ K (T_C), arises only in an incommensurate state, being in contrast with other RMn_2O_5 multiferroic members [11]. These properties render $NdMn_2O_5$ unique as a reference member of the RMn_2O_5 series to provide a deeper understanding of the fundamental mechanisms behind its magnetic and electric properties [15–18]. Doping this parent compound with smaller rare-earth elements, such as terbium (Tb), could enhance its multiferroic character. This would lead to significant changes in the structure of magnetic interactions, which can help in a better understanding of the strong magnetoelectric effect shown by RMn_2O_5 compounds. Besides, the coexistence of two rare-earth ions with different types of ground state, Kramers-like Nd^{3+} and non-Kramers Tb^{3+}, could lead to different types of site anisotropies. This also can provide more insight about the role of the *R*-Mn magnetic interactions in these systems and its large magnetocrystalline anisotropy that play a crucial role in determining the magnetocaloric properties of RMn_2O_5 multiferroics.

The main subject of this study is the $Nd_{0.8}Tb_{0.2}Mn_2O_5$ compound. A neutron diffraction study carried out recently on the here-studied $Nd_{0.8}Tb_{0.2}Mn_2O_5$ single crystals by Zobkalo *et al.* [19] reveals that two magnetic phases coexist over a broad temperature range, indicating magnetic phase separation. One of them bears features of $NdMn_2O_5$ (Nd phase) and the other one those of $TbMn_2O_5$ (Tb phase). The "Nd phase" features are closer to the magnetic order of $NdMn_2O_5$ with the same transition temperature $T_N = 30$ K. When compared to $NdMn_2O_5$, the $Nd_{0.8}Tb_{0.2}Mn_2O_5$ system exhibits even greater ability to generate ordered magnetic phases of the same type. Indeed, in the narrow temperature range of 20–30 K, two more magnetic incommensurate phases were observed [19]. The "Tb phase" has higher temperature of alignment than that of $NdMn_2O_5$, but lower than that of $TbMn_2O_5$. This inhomogeneity would arise from the nonrigidity of Mn^{3+}–Mn^{4+} bonding in the RMn_2O_5 multiferroics.

The presence of magnetic domains, on a short scale in a phase-separated sample, should affect locally the rare-earth crystal-field (CF) excitations by lifting its R^{3+} Kramers doublets (KD) degeneracy. Infrared transmission technique, combined with Raman spectroscopy, have been successfully used for the study of rare-earth crystal-field excitations and the interplay between charge, spin, and lattice degrees of freedom in manganite multifunctional materials [20–26]. In fact, relevant information concerning the local inhomogeneities, as well as the electronic and magnetic properties, can be obtained by studying the CF excitation and the phonon evolution as a function of temperature and/or magnetic field [25]. For instance, the Kramers ions Nd^{3+}, Sm^{3+}, and Dy^{3+} CF excitations have allowed the probing of *R*-Mn magnetic interactions in the multiferroic $NdMn_2O_5$, $SmMn_2O_5$, and $DyMnO_3$ [24,25]. Indeed, these Kramers ions, with odd numbers of electrons in their $4f$ shells, have levels with twofold degeneracies when they are placed at low site symmetry and exposed to the crystal-field effect induced by the surrounding oxygen ligands. Such Kramers degeneracies can only be lifted by an additional perturbation, which breaks the time-reversal invariance of the rare-earth ion Hamiltonian. This perturbation can be due to external magnetic fields or by an effective Zeeman effect resulting from local magnetic interactions. The high sensitivity of the Kramers-ion crystal-field levels to these perturbations is then a valuable probe for the existing magnetic exchange interactions.

In this paper, we present an optical and magnetic investigation of the multiferroic and the magnetocaloric properties of $Nd_{0.8}Tb_{0.2}Mn_2O_5$. The objectives are (i) to probe the nature of observed separated magnetic phases in $Nd_{0.8}Tb_{0.2}Mn_2O_5$, (ii) to provide a microscopic insight on the magnetocrystalline anisotropy in $Nd_{0.8}Tb_{0.2}Mn_2O_5$ while disclosing quantitatively its nature in all RMn_2O_5 systems, and (iii) to study the magnetocaloric effect in $Nd_{0.8}Tb_{0.2}Mn_2O_5$ and evaluate the contribution of coexisting magnetic phases.

II. EXPERIMENT

$Nd_{0.8}Tb_{0.2}Mn_2O_5$ single crystals were grown with the flux-melt method as described in Ref. [19]. This relatively moderate substitution of Nd^{3+} by Tb^{3+} (20%) is arbitrary chosen with the aim to induce significant changes in the electronic and magnetic properties of $NdMn_2O_5$. The crystallinity and the orientations of $Nd_{0.8}Tb_{0.2}Mn_2O_5$ samples are checked by x-ray diffraction (XRD) and Raman measurements. The XRD patterns are performed in the θ-2θ configuration of a PANalytical X'Pert PRO diffractometer with Cu Kα radiation operated at 45 kV and 40 mA. For Raman measurements, the samples were mounted on the cold finger of a microhelium Janis cryostat. The Raman spectra were collected between 5 and 300 K using a Labram-800 Raman spectrometer equipped with a nitrogen-cooled charge-coupled device detector and a proper notch filter. The excitation wavelength (632.8 nm) was focused on the samples using an objective lens of 50× with beam intensity maintained at less than 0.8 mW to avoid local heating. The infrared transmission spectra of $Nd_{0.8}Tb_{0.2}Mn_2O_5$ as a function of temperature were collected using a Fourier transform interferometer BOMEM DA3.002 equipped with a CaF_2 beamsplitter, a quartz-halogen source, and an InSb detector. For transmission measurements under magnetic fields, single crystals were placed in a cryostat equipped with a superconducting coil with the applied magnetic field along the *c* axis and parallel to the incident light propagation direction via light-pipe optics. These measurements were performed using a Bruker Vertex 80v infrared spectrometer. During the experiments, the temperature of the measured sample was kept at 4.2 K in a low-pressure helium gas. The magnetization curves were measured using a superconducting quantum interferometer device magnetometer from Quantum Design.

III. RESULTS AND DISCUSSION

A. X-ray diffraction patterns and Raman spectra of $Nd_{0.8}Tb_{0.2}Mn_2O_5$ versus those of $NdMn_2O_5$ and $TbMn_2O_5$

The RMn_2O_5 compounds crystallize in the orthorhombic structure [17] where edge-shared $Mn^{4+}O_6$ octahedra are

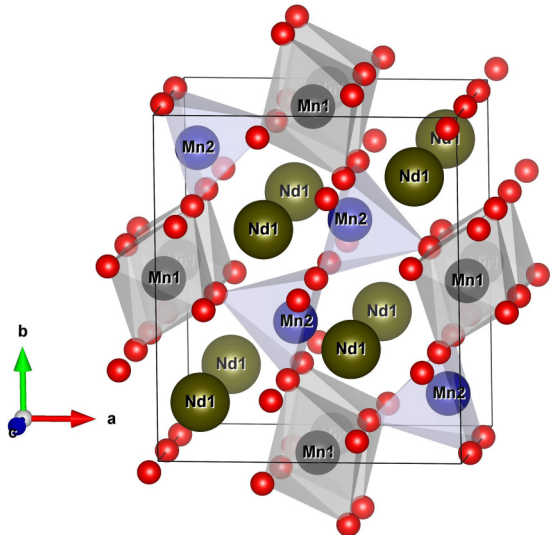

FIG. 1. Structure of RMn_2O_5. This schematic structure is generated by VESTA program. The oxygens O3 and O4 connect the octahedra and the pyramids along *a* and *b* axes, respectively. The O1 oxygen atoms link the pyramid pairs and the O2 oxygen atoms connect the octahedra along the *c* axis.

linked along the *c* axis and pairs of $Mn^{3+}O_5$ pyramids are connected to two $Mn^{4+}O_6$ chains as shown in Fig. 1. The rare-earth *R* ions are located in distorted RO_8 polyhedra. The space-group symmetry of RMn_2O_5 is usually identified as *Pbam*. However, recent findings have questioned the latter and identified a slight deviation from *Pbam* space group to be likely *Pm* [18]. Figure 2 shows θ-2θ scan of an XRD pattern of a face perpendicular to the *c* axis for $Nd_{0.8}Tb_{0.2}Mn_2O_5$, $NdMn_2O_5$, and $TbMn_2O_5$ single crystals. A zoom in on all the peaks is presented in the inset of Fig. 2. The presence of (002), (003), and (004) peaks confirms the crystal face orientation, and its high quality with a single domain. The reported XRD patterns allow us only to calculate the *c*-lattice constants. However, previous crystallographic studies carried

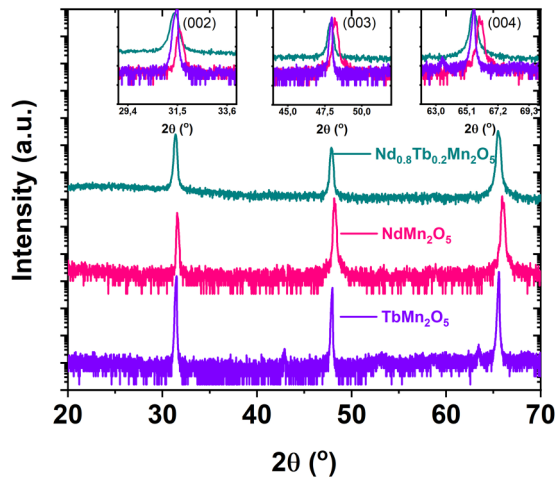

FIG. 2. θ-2θ scan of $Nd_{0.8}Tb_{0.2}Mn_2O_5$, $NdMn_2O_5$, and $TbMn_2O_5$ single crystals showing the diffracted peaks from the (00*l*) reflection planes. The intensity is presented in a logarithmic scale.

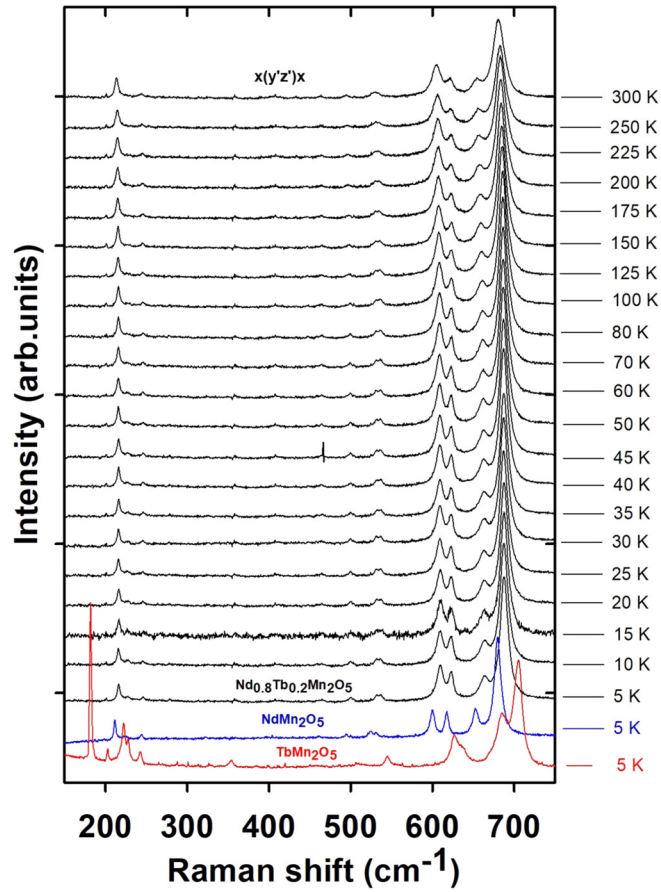

FIG. 3. Temperature dependence of the Raman spectra of $Nd_{0.8}Tb_{0.2}Mn_2O_5$ recorded in the $x(y'z')x$ polarization. The blue and the red curves show the Raman spectra of $NdMn_2O_5$ and $TbMn_2O_5$ at 5 K, respectively. The Raman spectra of $Nd_{0.8}Tb_{0.2}Mn_2O_5$ recorded in the $x(yz)x$ and $x(zz)x$ configurations are reported in the Supplemental Material [27].

out on our samples [16,19,24] have identified an orthorhombic structure with the *Pbam* space-group symmetry. The reported lattice constants *a*, *b*, and *c* are found to be 7.4940, 8.6071, and 5.6934 Å for $NdMn_2O_5$ (at 300 K); 7.531(5), 8.610(5), and 5.719(5) Å for $Nd_{0.8}Tb_{0.2}Mn_2O_5$ (at 3.8 K); and 7.351, 8.60, and 5.690 Å for $TbMn_2O_5$ (at 300 K), respectively. As expected, the volume of the unit cell is reduced when going from $NdMn_2O_5$ (367.233 $Å^3$) to $TbMn_2O_5$ (359.797 $Å^3$) as the size of the *R* ion is decreased.

Figure 3 presents the temperature dependence of $Nd_{0.8}Tb_{0.2}Mn_2O_5$ Raman spectra in the $x(y'z')x$ polarization. The details about the optical configurations of our Raman measurements are previously reported in Ref. [15]. The obtained Raman data in the $x(zz)x$ and $x(yz)x$ configurations are provided in the Supplemental Material (Fig. S1) [27]. Typical phonons associated with the orthorhombic RMn_2O_5 family are observed [23,24,28,29]. The phonons' linewidths are narrow, close to 4–10 cm^{-1}, confirming the high crystalline quality of our crystals. Besides, upon decreasing temperature down to 5 K, no additional vibration modes are observed, attesting to a structural phase stability. The Raman spectra of $Nd_{0.8}Tb_{0.2}Mn_2O_5$ are also compared to those of

TABLE I. Raman-active mode frequencies (in cm^{-1}) in $NdMn_2O_5$, $Nd_{0.8}Tb_{0.2}Mn_2O_5$, and $TbMn_2O_5$. "—" indicates that the vibration mode is not described in literature [29].

Ionic displacements [29]	Symmetry	$NdMn_2O_5$ 5 K	$Nd_{0.8}Tb_{0.2}Mn_2O_5$ 5 K	$TbMn_2O_5$ 5 K
—	$A_g(3)$	214	216	220
Symmetric bending due to Mn displacement.	$A_g(4)$	224	227	228
—	$A_g(8)$	497	499	506
—	$A_g(9)$	533	535	548
—	$A_g(10)$	601	609	627
Bending modes of Mn1-O3-Mn1 with predominant displacement of Mn1 ions.	$A_g(11)$	619	622	637
Symmetric stretch of Mn1-O3-Mn1 structural units due to oxygen displacements. Mn1-O4-Mn2 and Mn1-O3-Mn2 structural units: bond stretching modes due to O4 motion.	$A_g(12)$	681	688	704
Symmetric bending due to Mn displacement.	$B_{1g}(4)$	230	232	238
Symmetric bending due to Mn displacement.	$B_{1g}(5)$	323	324	327
Bending modes of Mn1-O3-Mn1 with predominant displacement of Mn1 ions.	$B_{1g}(12)$	655	663	683
Symmetric bending due to Mn displacement.	$B_{2g}(4)$	246	244	241
Asymmetric stretch caused by Mn1 movement. Symmetric bending due to Mn displacement.	$B_{2g}(5)$	292	295	300
—	$B_{2g}(6)$	346	348	349
Mn2-O1-Mn2 bending due to Mn2 displacements.	$B_{2g}(8)$	444	447	461
Mn2-O1-Mn2 bending involving predominant O1 motion.	$B_{2g}(9)$	454	458	471
—	$B_{3g}(5)$	275	277	279

$NdMn_2O_5$ (blue) and $TbMn_2O_5$ (red). Table I lists the phonon frequencies of $NdMn_2O_5$, $Nd_{0.8}Tb_{0.2}Mn_2O_5$, and $TbMn_2O_5$ crystals. The assignment of phonon symmetries and the ionic displacements is mainly based on the space-group analysis and the lattice dynamic calculations reported in Refs. [28] and [29]. Interestingly, our Raman data confirm that the here-investigated $Nd_{0.8}Tb_{0.2}Mn_2O_5$ sample is a single crystal and rule out unequivocally possible twinning. These findings are consistent with omega scans of some nuclear reflections in the basis plane $(h\ 0\ l)$ that were performed on our $Nd_{0.8}Tb_{0.2}Mn_2O_5$ crystals by Zobkalo *et al.* [19]. They have observed that the nuclear reflections correspond only to one crystallite. Except the vibration mode at 244 cm^{-1}, all the peak positions of $Nd_{0.8}Tb_{0.2}Mn_2O_5$ phonons, especially those at high frequencies mainly related to oxygen vibrations, are noticeably shifted to higher energy compared to those of $NdMn_2O_5$ and toward those of $TbMn_2O_5$. This frequency blueshift is in good agreement with the XRD data showing a reduction of the unit-cell volume when the size of the R ions is decreased due to smaller ⟨Mn1–O⟩ and ⟨Mn2–O⟩ bond distances [17]. The corresponding frequencies of the $B_{2g}(4)$ 244 cm^{-1} mode in $Nd_{0.8}Tb_{0.2}Mn_2O_5$ are 246 cm^{-1} in $NdMn_2O_5$ and 241 cm^{-1} in $TbMn_2O_5$. The frequency softening of this $B_{2g}(4)$ mode with increasing the Tb substitution is due to the fact that the latter involves mainly the vibration of rare-earth ions [29]. This softening is then caused by the increase of the reduced atomic mass of rare-earth [$m(\mathrm{Nd}) = 144.242\,u$ and $m(\mathrm{Tb}) = 158.925\,u$], since the squared frequency of this mode (ω^2) should scale, if one assumes a harmonic-oscillator-type motion, as $1/m(R)$.

Figures 4(a), 4(b), and 4(c) show the Raman frequencies of the $A_g(3)$, $A_g(10)$, $A_g(11)$, $B_{2g}(12)$, and $A_g(12)$ cm^{-1} modes as

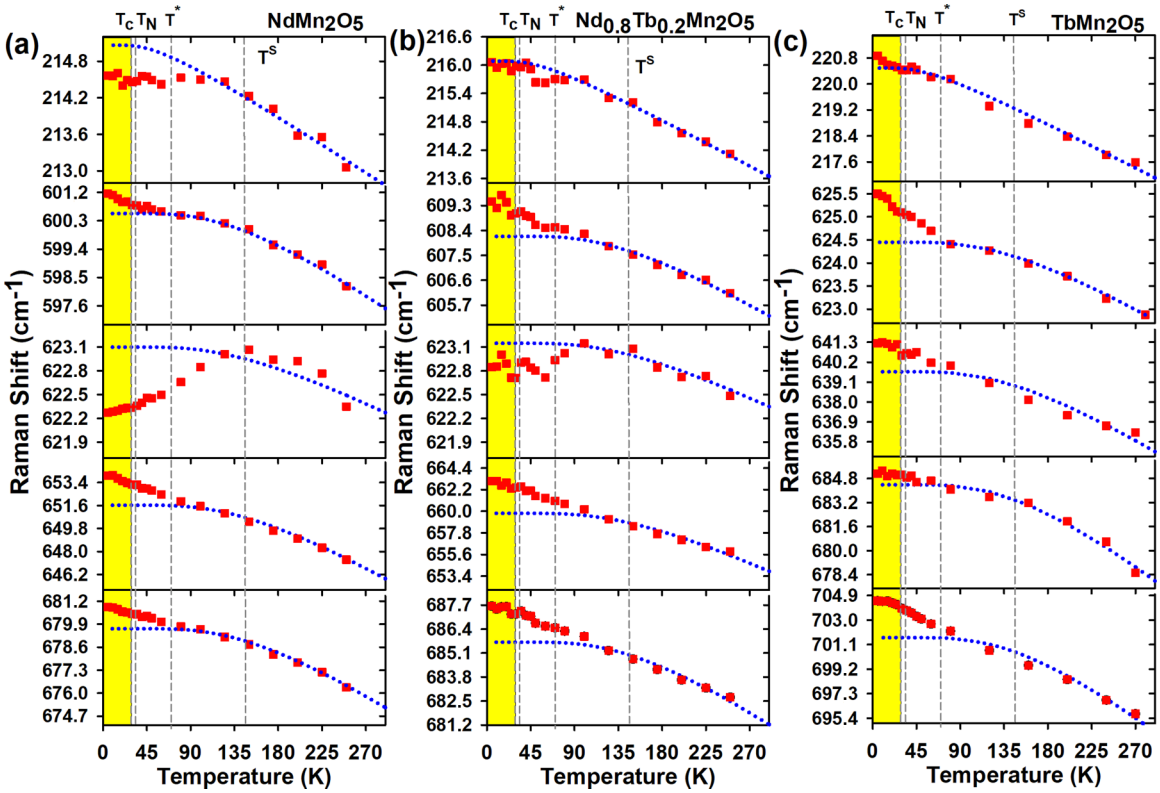

FIG. 4. Temperature dependence of the Raman frequencies of $A_g(3)$, $A_g(10)$, $A_g(11)$, $B_{1g}(12)$, and $A_g(12)$ modes in $NdMn_2O_5$, $Nd_{0.8}Tb_{0.2}Mn_2O_5$, and $TbMn_2O_5$. The dotted lines correspond to the expected anharmonic behavior. The characteristic temperatures T_C, T_N, T^*, and T^S are defined in the text.

a function of temperature for $NdMn_2O_5$, $Nd_{0.8}Tb_{0.2}Mn_2O_5$, and $TbMn_2O_5$, respectively. The dashed line is a fit of the experimental data at high temperature with the function $\omega(T) = \omega_0 - C(1 + \frac{2}{e^x - 1})$, where $x = \frac{\hbar\omega_0}{2K_BT}$, ω_0, and C are adjustable parameters. $\omega(T)$ describes the expected temperature dependence of a phonon mode frequency due to anharmonic phonon-phonon scattering. Based on such a behavior, the temperature dependence of some phonons exhibits evident anomalies around the characteristic temperatures $T^* \sim 70$ K and $T^S \sim 150$ K. The observed feature at T^S is attributed to a local disorder effect induced by the splitting of R–O bonds, into short and long bonds [30]. This thermal disorder is reduced at T^* when the number of short bonds matches up the number of long bonds in the unit cell. Interestingly, the Raman frequency of the ~622-cm^{-1} $A_g(11)$ mode for $NdMn_2O_5$ follows the anharmonic model between 300 and 160 K but decreases remarkably below $T^* \sim 70$ K. The frequency softening of this mode is very weak for $Nd_{0.8}Tb_{0.2}Mn_2O_5$. In contrast, this same mode shows a frequency-hardening behavior with respect to the anharmonic profile for $TbMn_2O_5$ below $T^* \sim 70$ K. Moreover, the magnitude of the frequency hardening of $A_g(10)$, A_g (12), and $B_{1g}(12)$ below $T^* \sim 70$ K ($\Delta\omega$ with respect to anharmonic prediction) is enhanced when decreasing the reduced R ions' size: $\Delta\omega \sim 1\,cm^{-1}$ for $NdMn_2O_5$, $\sim 2\,cm^{-1}$ for $Nd_{0.8}Tb_{0.2}Mn_2O_5$, and $\sim 3\,cm^{-1}$ for $TbMn_2O_5$. These different temperature evolutions of $A_g(10)$, $A_g(12)$, and B_{1g} (12) modes, involving mainly the vibration of Mn1-O3-Mn1 and Mn1-O4-Mn2 structural units (see Table I), indicate that doping $NdMn_2O_5$ with small Tb^{3+} ions (at 20%) induces noticeable changes in the lattice-dynamic properties. This would result in the modification of magnetic interactions at low temperatures opening the way for the coexistence of several magnetic propagation vectors.

B. Infrared study of the crystal-field excitations in $Nd_{0.8}Tb_{0.2}Mn_2O_5$

The temperature dependence of the rare-earth CF excitations provides useful information about the surrounding ligands and local inhomogeneities. In orthorhombic RMn_2O_5, the rare-earth R atoms occupy the C_s^{xy}-site symmetry. The oxygen environment and the interactions within the $4f^n$ electron configuration split the R^+ free-ion electronic levels. Each ^4I_J multiplet corresponds to $(2J + 1)/2$ sublevels for Kramers ions (Kramers doublets) and to $(2J + 1)$ for non-Kramers ions. The ^4I_J level multiplets of Nd^{3+} have total moments of $J = 9/2$, 11/2, 13/2, and 15/2 with their corresponding 5, 6, 7, and 8 Kramers doublets, respectively. The ^2F_J level multiplets of Tb^{3+} have total moments of $J = 6$, 5, 4, 3, 2, 1, and 0 with their corresponding 13, 11, 9, 7, 5, 3, and 1 degenerate levels, respectively. A complete identification of the CF level frequencies is necessary for the success of the numerical search for reliable CF parameters that depends strongly on the initial estimate. Figure 5 presents the transmission spectra of $NdMn_2O_5$, $Nd_{0.8}Tb_{0.2}Mn_2O_5$, and $TbMn_2O_5$ at 5 K for **E** parallel to the *ab* plane. In the transmission spectrum of $Nd_{0.8}Tb_{0.2}Mn_2O_5$, both the Nd^{3+} $(4f^3)$ $I_{9/2} \rightarrow I_{11/2}$, $I_{9/2} \rightarrow I_{13/2}$ and $I_{9/2} \rightarrow I_{15/2}$ CF transitions as well as the Tb^{3+} $(4f^8)$

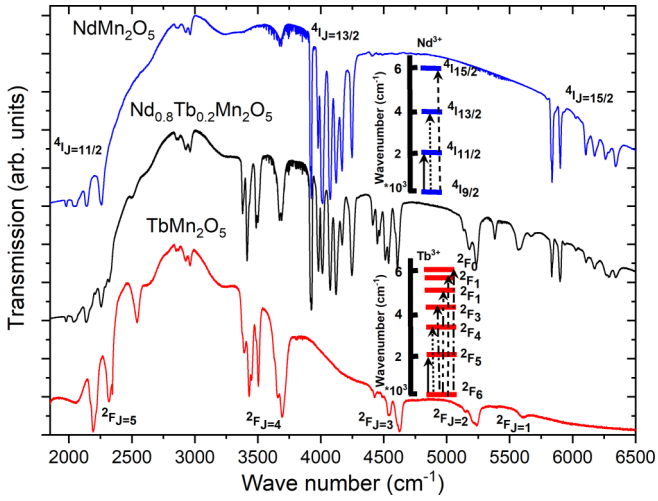

FIG. 5. The blue curve shows the transmission spectra of Nd^{3+} $^4I_{9/2} \rightarrow {}^4I_{11/2}$, $^4I_{3/2}$, and $^4I_{15/2}$ CF transitions in $NdMn_2O_5$ at 5 K. The red curve shows the transmission spectra of Tb^{3+} $^2F_6 \rightarrow {}^2F_5$, $^2F_4$, $^2F_3$, $^2F_2$, and $^2F_1$ CF transitions in $TbMn_2O_5$ at 5 K. The black curve shows the transmission spectra of Nd^{3+} and Tb^{3+} CF transitions in $Nd_{0.8}Tb_{0.2}Mn_2O_5$ at 5 K.

$F_6 \rightarrow F_5$, F_4, F_3, F_2, F_1, and F_0 CF transitions are found. As theoretically predicted, three groups of sharp absorption lines due to *f-f* transitions of Nd^{3+}, centered at 2200, 4000, and 6000 cm^{-1} are detected. These absorption bands correspond to the $I_{9/2} \rightarrow I_{11/2}$, $I_{9/2} \rightarrow I_{13/2}$, and $I_{9/2} \rightarrow I_{15/2}$ CF transitions. Some transmission spectra of all the absorption bands of Nd^{3+} ($^4I_9/2 \rightarrow {}^4I_J$) and Tb^{3+} ($^2F_6 \rightarrow {}^2F_J$) CF transitions in $Nd_{0.8}Tb_{0.2}Mn_2O_5$, recorded at different temperature between 300 and 5 K, are shown in the Supplemental Material (Fig. S2) [27]. Table II compares the CF energy levels of the 26 Kramers doublets of Nd^{3+} in $Nd_{0.8}Tb_{0.2}Mn_2O_5$ with those in $NdMn_2O_5$ at 30 K, while Table III compares the CF energy levels of Tb^{3+} in $Nd_{0.8}Tb_{0.2}Mn_2O_5$ with respect to those in $TbMn_2O_5$ at 30 K. The ground-state excited levels of Nd^{3+} ($I_{9/2}$) and Tb^{3+} (F_6) are determined when they are thermally populated at high temperatures (above 100 K). Their energy values are deduced by comparing the thermally excited levels of the different multiplets. The CF energy levels of Nd^{3+} in $Nd_{0.8}Tb_{0.2}Mn_2O_5$ are quite similar to those in $NdMn_2O_5$. Small redshifts (lower than ~2–5 cm^{-1}) are only observed for some CF energy levels (excitations at 2141, 2257, 5900, and 6174 cm^{-1}). These small differences in the CF energy levels mean that substituting the Nd ions by the smaller Tb ions (at 20%) in $NdMn_2O_5$ does not significantly change the Nd surrounding oxygen atoms in NdO_8 (the average Nd–O distances ($\langle$Nd–O$\rangle$) could be slightly expanded). This slight change is in agreement with the small redshift (~ 2 cm^{-1}) of the Raman phonon at 246 cm^{-1} involving the *R*-ion vibrations. These findings reveal that the Nd Kramers doublets is only sensitive to the change induced by local magnetic perturbations in $Nd_{0.8}Tb_{0.2}Mn_2O_5$, which are induced by the magnetic moments of Tb ions. In contrast, the CF energy levels of Tb^{3+} in $Nd_{0.8}Tb_{0.2}Mn_2O_5$ are notably shifted when compared to those in $TbMn_2O_5$: large redshifts (~ 30 cm^{-1}) are observed for some CF energy levels such as those at 3670, 3694, 4512, 5178, and 5564 cm^{-1} (see Table III). The Tb^{3+} $^2F_6 \rightarrow {}^2F_4$ and $^2F_6 \rightarrow {}^2F_3$ CF transitions in $Nd_{0.8}Tb_{0.2}Mn_2O_5$ compared to those in $TbMn_2O_5$ measured at 5 K with the same polarization E//*ab* plane are reported in Fig. S3 [27]. The shape of absorption bands is also affected as the spectral weight of some CF excitations in $Nd_{0.8}Tb_{0.2}Mn_2O_5$ compared to those in $TbMn_2O_5$ is redistributed. For example, see the absorption bands at 3388, 3415, 3431, 4448, and 4467 cm^{-1}. All these observations indicate that the Tb surrounding oxygen atoms (TbO_8) in $Nd_{0.8}Tb_{0.2}Mn_2O_5$ is significantly distorted when compared to that in $TbMn_2O_5$. In addition, the large redshifts of Tb^{3+} CF energy levels in $Nd_{0.8}Tb_{0.2}Mn_2O_5$ implies that the average Tb–O distances $\langle$Tb–O$\rangle$ are significantly expanded compared to that in $TbMn_2O_5$.

The temperature dependence of the frequency and the full width at half maximum (FWHM) of the 3922-cm^{-1} CF excitation in $Nd_{0.8}Tb_{0.2}Mn_2O_5$, between 300 and 35 K, are reported in Figs. S4(a)–S4(b) [27]. $NdMn_2O_5$ data are also shown for comparison. As shown, a similar temperature dependence is observed. In fact, the frequency of the 3922-cm^{-1} CF excitation hardens between 300 and 200 K and becomes nearly constant between 200 and 70 K. Below 70 K, it hardens again while its FWHM decreases gradually in the temperature range going from 300 to 70 K and then increases between 70 and 30 K. Such a behavior is observed for all the Nd^{3+} CF excitations. This broadening of the CF excitations below 70 K, recently reported for the, Sm^{3+}, Tb^{3+}, and Ho^{3+} CF excitations in $SmMn_2O_5$, $TbMn_2O_5$, and $HoMn_2O_5$ [24,25] is attributed to a local thermal disorder effect. The latter is induced by the splitting of *R*–O bonds, which also explains the decrease in Raman intensities, and the frequency shifts of some RMn_2O_5 phonons below 180 K. This thermal disorder effect in the RO_8 polyhedra seems to be a universal behavior

TABLE II. Experimental CF excitation energies (in cm^{-1}) at 30 K of the Kramers doublets of Nd^{3+} in $NdMn_2O_5$.

Nd^{3+} CF levels in	$^4I_{9/2}$	$^4I_{11/2}$	$^4I_{13/2}$	$^4I_{15/2}$
$NdMn_2O_5/Nd_{0.8}Tb_{0.2}Mn_2O_5$	0	1978/1978	3921/3922	5835/5833
	142/141[a]	2035/2035	3978/3978	5900/5898
	238/238[a]	2043/2043	4011/4011	6104/6104
	291/290[a]	2055/2054	4074/4073	6174/6172
	329/329[a]	2141/2136	4120/4119	6196/6196
		2257/2255	4168/4168	6262/6262
			4246/4245	6289/6289
				6344/6344

[a]The energy of these crystal-field excitations is determined at high temperature when they are thermally populated.

TABLE III. CF energy levels of Tb^{3+} in $Nd_{0.8}Tb_{0.2}Mn_2O_5$ with respect to those in $TbMn_2O_5$ at 30 K.

Tb^{3+}CF levels in $Nd_{0.8}T_{0.2}bMn_2O_5/TbMn_2O_5$						
$F6$	$F5$	$F4$	$F3$	$F2$	$F1$	$F0$
0	2165/2173	3379/3379	4413/4426	5132/5144	5564/5596	5939/
/18	2185/2192	3388/3392	4448/4460	5178/5207	5592/5617	
/37	2210/2219	3415/3430	4467/4486	5232/5235	5672/	
65/75	2294/	3431/3453	4512/4535	5246/5249		
105/120	2319/2319	3485/3485	4539/4549	5383/5394		
138/143	2329/	3503/3505	4590/4606			
150/180	2510/2510	/3638	4609/4628			
		3670/3700				
		3694/3721				

regarding the lattice-dynamic properties of RMn_2O_5 series and raises questions concerning the actual space-group symmetry of RMn_2O_5 systems at high temperature as previously discussed by Baledent *et al.* [18]. Keeping this in mind, further experimental and numerical investigations are still needed to learn more about the role of thermal dynamic properties of the R–O bonds in driving the ferroelectric properties of RMn_2O_5 systems.

Figure 6 shows the absorbance maps of Nd^{3+} $I_{9/2} \rightarrow I_{13/2}$ CF transitions in $Nd_{0.8}Tb_{0.2}Mn_2O_5$ as a function of temperature, between 45 and 4.5 K, compared to those in $NdMn_2O_5$. The absorbance spectra (A) are calculated from the transmission spectra (T) and the incident intensity (I_0) using the equation $A = -\log_{10}(T) = -\log_{10}(\frac{I}{I_0})$. The variation of the $^4I_1$ 3/2 CF excitation frequencies as a function of temperature is presented by the empty white squares. With decreasing temperature, the CF lines in $Nd_{0.8}Tb_{0.2}Mn_2O_5$ similarly behave as those in $NdMn_2O_5$ while the different CF excitations are equally split compared to their positions at 35 K. The temperature profile of the splitting shift is almost the same for all the CF excitations. An example illustrating this evident splitting is presented in Fig. S5 for the absorption band at 3922 cm^{-1} (3921 cm^{-1}) of Nd^{3+} in $Nd_{0.8}Tb_{0.2}Mn_2O_5$ ($NdMn_2O_5$) [27]. Below 35 K (30 K), this band is well resolved in two subbands at 3918 cm^{-1} (3918 cm^{-1}) and 3925 cm^{-1} (3923 cm^{-1}). As discussed for the CF energy levels of Nd^{3+} in $NdMn_2O_5$ [15], the uniform splitting of the Nd^{3+} CF excitations in $Nd_{0.8}Tb_{0.2}Mn_2O_5$ is also due to the degeneracy of the KD ground state of Nd^{3+}. This degeneracy (Δ_0) is induced by an effective Zeeman effect resulting from the Nd-Mn exchange interaction below the antiferromagnetic ordering of Mn moments. Figure 7 shows the variation of the splitting $\Delta_0(T)$ as a function of temperature in both $Nd_{0.8}Tb_{0.2}Mn_2O_5$ and $NdMn_2O_5$. Similar temperature dependence of $\Delta_0(T)$ is observed. The ground-state KD of Nd^{3+} in $Nd_{0.8}Tb_{0.2}Mn_2O_5$ ($NdMn_2O_5$) is affected when the temperature is lowered from 30 to 5 K. Indeed, the average doublet splitting increases from 7 cm^{-1} at 30 K (5.5 cm^{-1} at 28 K) to ~9 cm^{-1} (7.5 cm^{-1}) at 5 K. However, the magnitude of $\Delta_0(T)$ in $Nd_{0.8}Tb_{0.2}Mn_2O_5$ is relatively larger than that in $NdMn_2O_5$. In addition, the corresponding temperature to the splitting of KD ground state is shifted to a higher temperature. For $Nd_{0.8}Tb_{0.2}Mn_2O_5$ the splitting is observed below 35 K while it occurs only below 30 K for $NdMn_2O_5$. In $NdMn_2O_5$ [15], the splitting of Nd^{3+} KD ground state is observed at the occurrence of the ferroelectric phase transition, indicating that the Nd^{3+} ions and Nd-Mn interactions are involved in the magnetic and ferroelectric orderings at low temperatures. The observed relatively high value of the ground-state Nd-Mn exchange splitting (9 cm^{-1}), at higher temperature, could be responsible for the stability of Nd magnetic phase (Nd phase) in

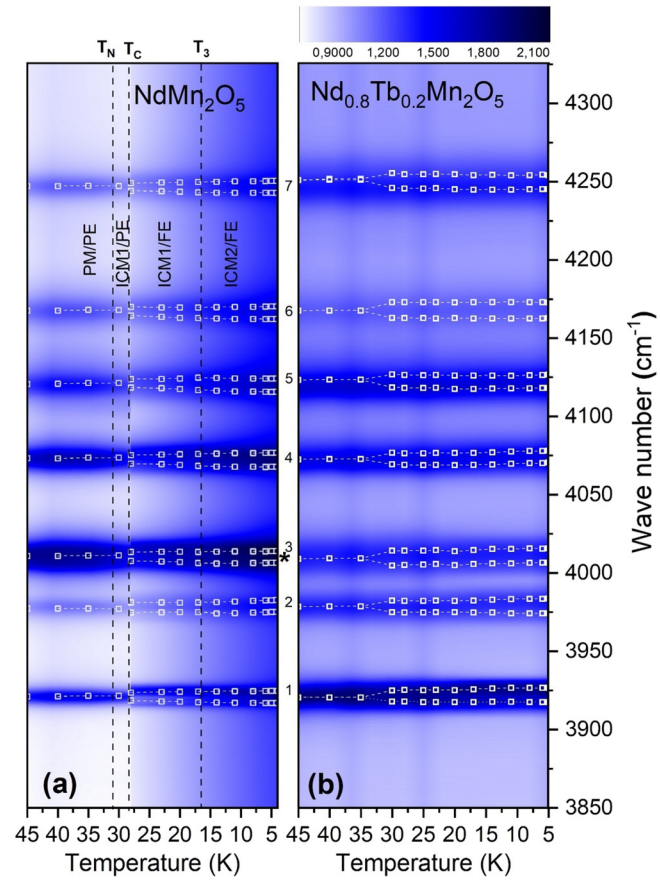

FIG. 6. Absorbance maps of Nd^{3+} $I_{9/2} \rightarrow I_{13/2}$ CF transitions as a function of temperature, between 45 and 4.5 K, in $NdMn_2O_5$ (a) and in $Nd_{0.8}Tb_{0.2}Mn_2O_5$ (b), where the empty white squares indicate the CF frequency levels of the $^4I_{13/2}$ multiplet. The notations PM, PE, ICM, CM, and FE are used to represent paramagnetic, paraelectric, incommensurate magnetic, commensurate magnetic, and ferroelectric states. (a) was previously reported in our paper on $NdMn_2O_5$ [15]. The vertical dashed lines indicate the temperature of the different phase transitions.

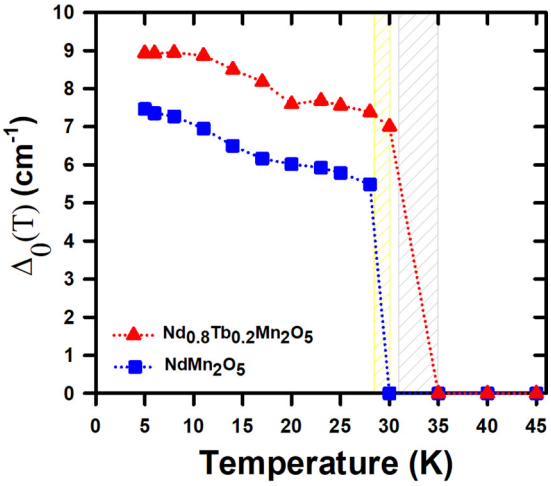

FIG. 7. Variation of the splitting $\Delta_0(T)$ as a function of temperature in $NdMn_2O_5$ and in $Nd_{0.8}Tb_{0.2}Mn_2O_5$.

$Nd_{0.8}Tb_{0.2}Mn_2O_5$. We spectulate that the ferroelectic character of Nd phase is enhanced and its contribution to the total spontaneous polarization of $Nd_{0.8}Tb_{0.2}Mn_2O_5$ is improved. However, ferroelectric measurements must be prformed to confirm these inferences. On the other hand, the magnetic anisotropy in $Nd_{0.8}Tb_{0.2}Mn_2O_5$ should be necessarily enhanced compared to $NdMn_2O_5$ due to the ordering of Tb magnetic moments within the *ab* plane. This means that the Zeeman effect on the *i*th Nd CF excitations, along the *c* axis, should be reduced since it depends on the Zeeman-splitting *g* tensors (the gyromagnetic g_z factor along the *c* axis) [31], which is sensitive to the magnetic anisotropy. In the basis quantized along one of the main magnetic axes, the main values of the *g* tensor obey the relations $g_x = g_y = g_z = g$ for cubic and icosahedral groups and $g_x = g_y = g_\perp$, $g_z = g_{||}$ for axial groups [31]. To get a microscopic insight on the magnetic anisotropy change in $Nd_{0.8}Tb_{0.2}Mn_2O_5$, the magnetic field dependence of Nd^{3+} CF transitions are studied and compared to that reported in $NdMn_2O_5$. Figure 8 (Fig. S6 in Supplemental Material [27]) presents the absorption bands of Nd^{3+} $\mathbf{I_{9/2}} \rightarrow \mathbf{I_{11/2}}$ ($\mathbf{I_{9/2}} \rightarrow \mathbf{I_{13/2}}$) CF transitions as a function of magnetic field ($\mathbf{B}||c$), between 0 and 11 T, in $Nd_{0.8}Tb_{0.2}Mn_2O_5$ [Fig. 8(a)] and $NdMn_2O_5$ [Fig. 8(b)] at 4.2 K. As expected, additional splittings due to the Zeeman effect are observed. The high-energy Kramers-doublets component of the ground state at 4.2 K is very weakly populated and does not contribute to the CF excitations. This means that the detected splittings are directly related to the KD excited multiplets. The magnetic field dependence of the crystal-field level scheme for the $^4I_{11/2}$ and $^4I_{13/2}$ multiplets of Nd^{3+} ions in $Nd_{0.8}Tb_{0.2}Mn_2O_5$ is remarkably different from that of the $NdMn_2O_5$ parent compound. Interestingly, except the CF excitations at 1979 cm^{-1}, which do not split in $NdMn_2O_5$ while splitting in $Nd_{0.8}Tb_{0.2}Mn_2O_5$, all the CF excitations, which split significantly in $NdMn_2O_5$, are weakly split under high magnetic fields in $Nd_{0.8}Tb_{0.2}Mn_2O_5$. For example, the CF excitations at 2260 and 4250 cm^{-1}, which show an important splitting of 50 and 70 cm^{-1} (11 T) in $NdMn_2O_5$, exhibit no significant splitting in $Nd_{0.8}Tb_{0.2}Mn_2O_5$ (broadened by $\sim$3 cm^{-1} under 11 T), respectively.

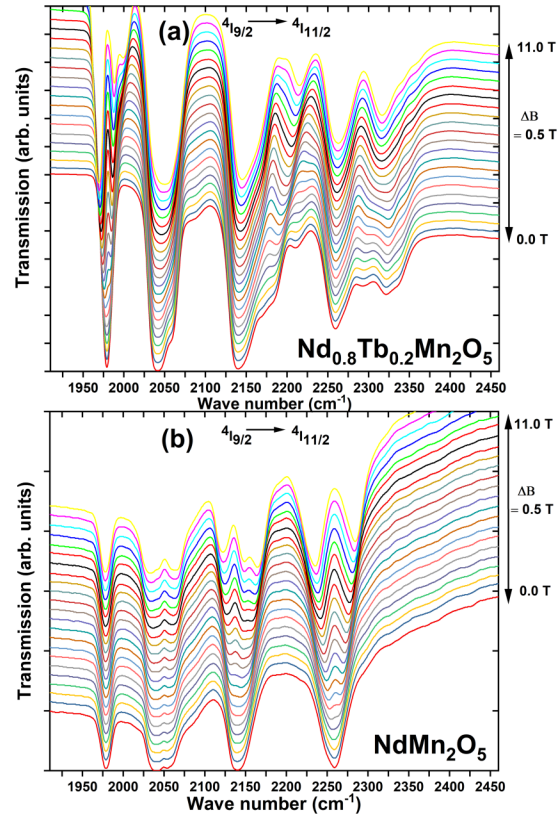

FIG. 8. Absorption bands of Nd^{3+} $\mathbf{I_{9/2}} \rightarrow \mathbf{I_{11/2}}$ CF transitions as a function of magnetic ($\mathbf{B}||c$) field, between 0 and 11 T, in $NdMn_2O_5$ (a) and in $Nd_{0.8}Tb_{0.2}Mn_2O_5$ (b) at 4.2 K.

According to Hemberger *et al.*, the doublet splitting $2\Delta_i$ of the *i*th CF Kramers doublet can be determined by [32]

$$\Delta_i^2 \approx \left(\Delta_z^{ex} A_{zi}\right)^2 + \left(\Delta_x^{ex} A_{xi} + g_z \mu_B H_z\right)^2,$$

where A_{xi} and A_{zi} are normalized components of the antiferromagnetic vector of the *i*th Mn ions in the *ac* plane. $(\Delta_z^{ex} A_{zi})$ and $(\Delta_x^{ex} A_{xi})$ are the Nd-Mn exchange splitting for $A||x$ and $A||z$ axis, respectively. g_z represents the *z* component of the g tensor. *x*, *y*, and *z* correspond to the *a*, *b*, and *c* axes, respectively. In this framework, the very weak splitting of excited KD under magnetic fields in $Nd_{0.8}Tb_{0.2}Mn_2O_5$ indicates that the *z* component of *g* tensor, $g_{||} = g_z$ factor, is lower when compared to that of $NdMn_2O_5$.This means that the magnetic anisotropy is enhanced with the partial substitution of Nd^{3+} ions by Tb^{3+} ions at 20%. This also indicates that the Nd^{3+} spins (and necessarily the Tb^{3+} spins) are more ordered within the *ab* plane.

C. Magnetocrystalline anisotropy and rotating magnetocaloric effect in $Nd_{0.8}Tb_{0.2}Mn_2O_5$

Although the magnetocaloric effect (MCE) is generally considered in the community as an "applied" measurement tool to characterize magnetic refrigerant materials [7–9], the MCE is also shown to be a useful method to probe the subtle balance of coexisting phases in mixed-phase manganites [33]. The purpose of this section is to investigate the magnetocaloric properties of $Nd_{0.8}Tb_{0.2}Mn_2O_5$ with a great attention

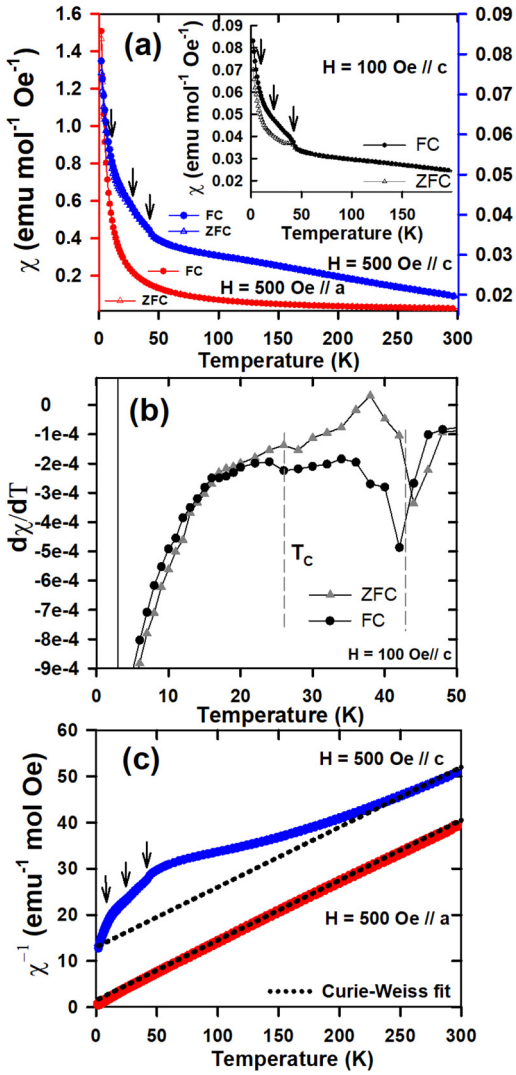

FIG. 9. (a) Temperature dependence of the magnetic susceptibility *M/H* of a $Nd_{0.8}Tb_{0.2}Mn_2O_5$ single crystal measured in ZFC and FC conditions with an applied magnetic field of 500 Oe along the *a*- and *c* axes. Inset: the magnetic susceptibility with an applied magnetic field of 100 Oe along the *c* axis. Triangle and circle symbols indicate susceptibility data measured in ZFC and FC processes, respectively. (b) The derivative of χ along the *c* axis. (c) Curie-Weiss fitting of the inverse susceptibility as a function of temperature and with an applied magnetic field of 500 Oe along the *a*- and *c* axes.

paid to its rotating MCE. The obtained results are analyzed and compared to those reported for the parent compound $TbMn_2O_5$ [7]. This mainly enables us to get insight regarding the role of magnetocrystalline anisotropy in determining the rotating MCE in the RMn_2O_5 family.

Figure 9(a) shows the temperature dependence of the magnetic susceptibility *M/H* of a $Nd_{0.8}Tb_{0.2}Mn_2O_5$ single crystal measured in zero-field cooled (ZFC) and field-cooled (FC) conditions with an applied magnetic field of 500 Oe along the *a*- and *c* axes. Inflection points as kinklike anomalies are observed, as indicated by arrows in Figs. 9(a) and 9(c). The inset represents the magnetic susceptibility with an applied magnetic field of 100 Oe along the *c* axis. A large hysteresis is observed between the ZFC and FC curves in the temperature range between ∼43 and ∼20 K. Figure 9(b) presents the derivative of χ along the *c* axis compared to that of $NdMn_2O_5$. The derivative process determines approximatively the temperatures corresponding to the kinklike anomalies which are located around 43, 26, and 8 K. Here, the nature of these anomalies is explained regarding the recent neutron diffraction study carried out on our crystals and reported by Zobkalo *et al.* [19]. The anomaly around 43 K could be attributed to a precursor effect of the long-range Mn magnetic order at 37 K. The coexistence of magnetic phase separation in $Nd_{0.8}Tb_{0.2}Mn_2O_5$, closer to the magnetic orders in $NdMn_2O_5$ (Nd phase) and $TbMn_2O_5$ (Tb phase), makes its phase magnetic diagram rich on account to the competition between different exchange interactions. The anomaly at 26 K, also observed in $NdMn_2O_5$ and coinciding with the appearance of its ferroelectric character, could be related the Mn spin reordering. The 8 K feature is probably due to the ordering of the rare-earth spins as usually observed in this series of compounds. The large hysteresis, between the ZFC and FC curves, is due to the multiple-*k* incommensurate magnetic structure observed in $Nd_{0.8}Tb_{0.2}Mn_2O_5$ over the same temperature range. These multiple competing magnetic interactions could arise from the nonrigidity of the Mn^{3+}–Mn^{4+} bonding and the geometrical arrangement of the superexchange interactions.

Figure 9(c) presents a Curie-Weiss fitting of the inverse susceptibility. Well above T_N, the inverse susceptibility follows the Curie-Weiss behavior $\chi^{-1}=\frac{T-\theta_{CW}}{C}$ (dashed lines), yielding to an effective magnetic moment value of $\mu_{ob} \approx 7.84\,\mu_B$ that is closer to the theoretical value given by $\mu_{eff}=\sqrt{[0.8\,\mu_{eff}(Nd^{3+})]^2+(0.2\mu_{eff}(Tb^{3+}))^2+\mu^2_{eff}(Mn^{3+})+\mu^2_{eff}(Mn^{4+})}=7.15\mu_B$. By considering the demagnetization factor, the obtained value of of θ_{CW} along the *c* axis is roughly −102 K, suggesting dominant antiferromagnetic interactions. In contrast, the value of θ_{CW} along the *a* axis is about −11 K, indicating a strong magnetocrystalline anisotropy in $Nd_{0.8}Tb_{0.2}Mn_2O_5$. According to Hur *et al.* [34], RMn_2O_5 compounds exhibit a strong magnetocrystalline anisotropy, and their easy directions depend on the size of *R* ions. The easy magnetic direction was found to be along the *b* axis for $DyMn_2O_5$ [34] and $HoMn_2O_5$ [8], while it is along the *a* axis for $TbMn_2O_5$ [2]. For $ErMn_2O_5$ [35], $TmMn_2O_5$ [36], and $YbMn_2O_5$ [37], the easy magnetization orientation is along the *c* axis. However, in $GdMn_2O_5$, no magnetocrystalline anisotropy between the main crystallographic axes is observed [38,39]. Concerning light rare-earth ions, the easy magnetization direction in $NdMn_2O_5$ is along the *ab* plane [14] since no significant anisotropy occurs between the *a* and *b* directions. For the $SmMn_2O_5$ compound, the easy axis is parallel to the *c* direction. At low temperatures, Blake *et al.* [40] has shown that the spin structures of RMn_2O_5 mainly differ in their periodicity along the *c* axis, which was attributed to the change of the *R* radius that determines also the sign of the magnetic exchange between adjacent planes. However, the nature of magnetocrystalline anisotropy in the RMn_2O_5 family, already manifested in the paramagnetic phase, is not clear and still needs investigation. Here, the role of the anisotropic charge distribution of their $4f$ shells in determining the anisotropic magnetic properties of RMn_2O_5

compounds is addressed by studying the dependence of $\theta_{||} - \theta_{\perp}$ sign on the atomic number of the rare earth. Indeed, the sign of the difference $\theta_{||} - \theta_{\perp}$ is determined by the sign of the Stevens factor α_J, which is a measure of the quadrupolar charge distribution (prolate or oblate shape) within the R ion, itself determined by the crystal field. This approach has been successfully used to explain the origin of the magnetocrystalline anisotropy in the ferroic hexagonal RMnO$_3$ oxides with heavy rare-earth elements [41]. Below, we adopt this formalism to the multiferroic RMn$_2$O$_5$ oxides with both heavy and light rare-earth ions.

According to the Elliott formula, the difference $\theta_{||} - \theta_{\perp}$ can be written as

$$\theta_{||} - \theta_{\perp} = -\tfrac{3}{10}(2J-1)(2J+3)\alpha_J A_{20}\langle r^2\rangle, \tag{1}$$

where $\langle r^2\rangle$ is the $4f$ radial expectation value, A_{20} is the rare-earth crystal-field parameter, and α_J is the Stevens factor. We consider the ground configuration $4f^N$, where N is the number of $4f$ electrons ($1 < N < 14$). The quantum numbers S, L, and J, regarded as continuous variable, can be expressed in terms of N by the means of the three Hund rules:

$$S = \tfrac{1}{2}(14-N) \text{ for heavy RE} \tag{2}$$

$$S = \tfrac{1}{2}N \text{ for light RE} \tag{3}$$

$$L = S(N-7) = \tfrac{1}{2}(14-N)(N-7) \text{ for heavy RE} \tag{4}$$

$$L = S(7-N) = \tfrac{1}{2}N(7-N) \text{ for light RE} \tag{5}$$

$$J = L + S = \tfrac{1}{2}(N-6)(14-N) \text{ for heavy RE} \tag{6}$$

$$J = L - S = \tfrac{1}{2}N(6-N) \text{ for light RE} \tag{7}$$

For the Stevens factor of a heavy rare-earth ion the following expression holds [42]:

$$\alpha_J = \frac{2}{45}\,\frac{L(7-4S)}{J(2J-1)} \text{ for heavy RE} \tag{8}$$

$$\alpha_J = -\frac{2}{45}\,\frac{(7-4S)}{(2L-1)}\,\frac{(L+1)(2L+3)}{(J+1)(2J+3)} \text{ for light RE} \tag{9}$$

where the "−" sign is used in the first half of the shell and the "+" sign is used in the second half of the shell. By writing J and α_J as a function of N, $\theta_{||} - \theta_{\perp}$ can be expressed as follows:

$$\theta_{||} - \theta_{\perp} = \tfrac{1}{75} f'_N A_{20}\langle r^2\rangle \text{ for heavy RE} \tag{10}$$

$$\theta_{||} - \theta_{\perp} = \tfrac{1}{75} f''_N A_{20}\langle r^2\rangle \text{ for light RE} \tag{11}$$

where

$$f'_N = (N-7)(2N-21)\left(N - 14 - \frac{3}{N-6}\right) \text{ for heavy R} \tag{12}$$

$$f''_N = \frac{[N(6-N)-1](7-2N)[N(7-N)+2]\,[N(7-N)+3]}{[N(6-N)+2][N(7-N)-1]} \times \text{ for light RE} \tag{13}$$

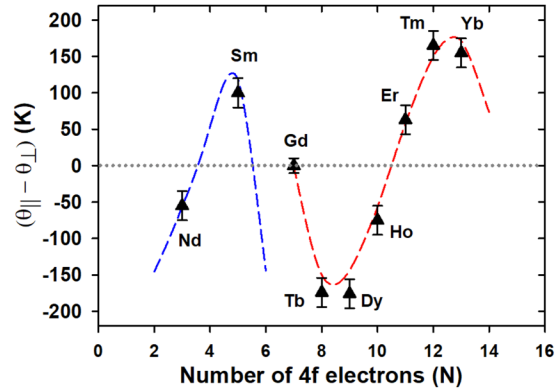

FIG. 10. Dependence of $(\theta_{||} - \theta_{\perp})$ sign on the atomic number (N) of $4f$ electrons in the ground configuration of R^{3+} rare-earth elements. The dashed blue and red curves represent Eqs. (12) and (13), respectively (times –4 K). The number N is regarded as a continuous variable. The experimental data of $(\theta_{||} - \theta_{\perp})$ (triangle symbol) for NdMn$_2$O$_5$, SmMn$_2$O$_5$, TbMn$_2$O$_5$, and HoMn$_2$O$_5$ are determined from our magnetization measurements, while those for GdMn$_2$O$_5$, DyMn$_2$O$_5$, ErMn$_2$O$_5$, TmMn$_2$O$_5$, and YbMn$_2$O$_5$ are deduced from Refs. [8,35–39].

According to this prediction, the quantity $\theta_{||} - \theta_{\perp}$ should have the same dependence on N as the numerical factors f'_N (for heavy RE) and f''_N (for light RE). Figure 10 shows the dependence on N of the quantity $\theta_{||} - \theta_{\perp}$, where the dashed red and blue lines represent Eqs. (12) and (13) (times −4 K), respectively. The crystal-field parameter $A_{20}\langle r^2\rangle$ is fixed at $A_{20}\langle r^2\rangle = -300$ K. As shown, a good agreement, including a change of sign between $N = 3$ (Nd^{3+}) and 5 (Sm^{3+}) and between $N = 10$ (Ho^{3+}) and 11(Er^{3+}), can be clearly observed. In addition, the absence of anisotropy for Gd^{3+} magnetic moments (f'_N is zero for Gd^{3+}) confirms Sanina *et al.*'s findings [38,39]. This demonstrates that the anisotropic magnetic properties of RMn$_2$O$_5$ at high temperatures are predominantly governed by the second-order crystal field on the rare-earth sites.

The isothermal $M(H)$ curves of the Nd$_{0.8}$Tb$_{0.2}$Mn$_2$O$_5$ single crystal measured as a function of magnetic field applied along the easy and hard axes are plotted in Figs. 11(a) and 11(b), respectively. Along the easy axis a, the magnetization isotherms demonstrate a typical "ferromagnetic" behavior at the temperatures below the Néel transition temperature of Tb (T_{Tb}), while the linear field dependence of the magnetization at high temperatures is typical for a "paramagnetic phase." The temperature dependence of isothermal entropy change (ΔS) due to the variation of applied magnetic field is the most-used parameter for evaluating the magnetocaloric potential of magnetic materials [43]. In an isothermal process of magnetization, ΔS can be obtained from isotherms $M(H)$ curves by using the well-known Maxwell relation,

$$\Delta S(T, 0 \to H) = \int_0^H \left(\frac{\partial M}{\partial T}\right)_{H'} dH'. \tag{14}$$

Due to the discreteness of the data, the ΔS values are usually computed by the following numerical

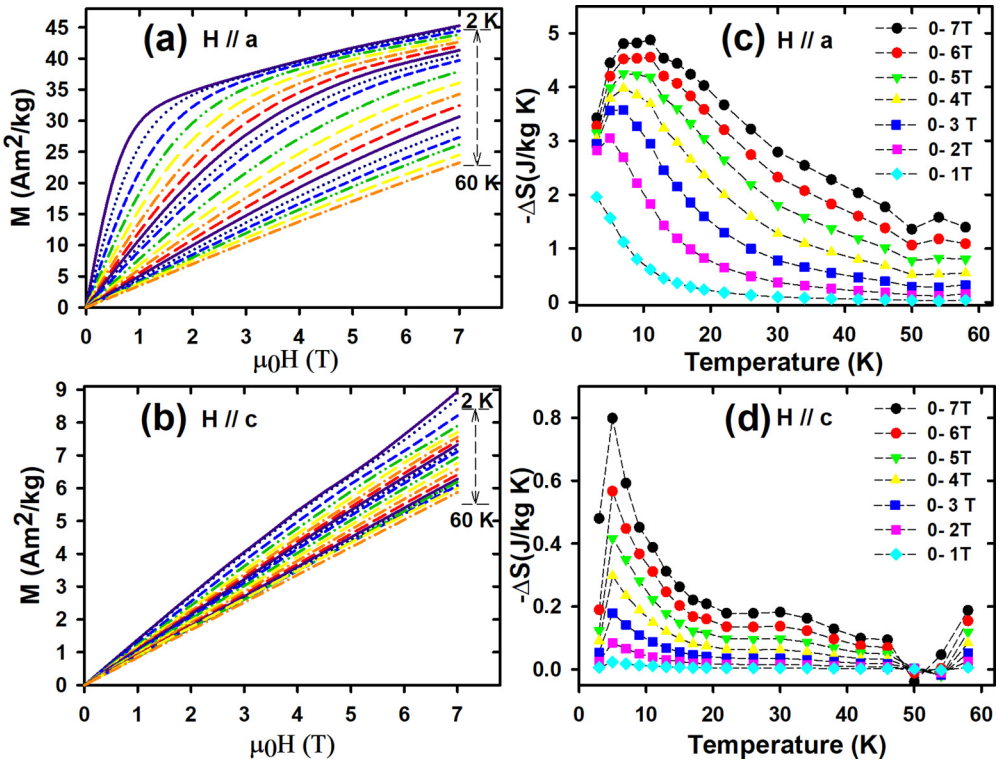

FIG. 11. (a), (b) Isothermal magnetization curves of the single-crystal $Nd_{0.8}Tb_{0.2}Mn_2O_5$ measured as a function of magnetic field applied along the *a*- and *c* axes at different fixed temperatures. (c), (d) Computed value of $-\Delta S$ as a function of temperature under several external magnetic fields along the *a*- and *c* axes.

formula:

$$\Delta S = \sum_i \frac{M_{i+1} - M_i}{T_{i+1} - T_i} \Delta H_i, \tag{15}$$

where M_{i+1} and M_i are the measured magnetizations in a field H, at temperatures T_{i+1} and T_i, respectively. Figures 11(c) and 11(d) show the computed value of $-\Delta S$ as a function of temperature under several external magnetic fields along the *a* and *c* axes in $Nd_{0.8}Tb_{0.2}Mn_2O_5$. As shown, the isothermal entropy change also reveals a considerable anisotropy. For *H//a*, the $-\Delta S$ maxima are distributed in the temperature range between ∼5 and ∼15 K. When changing the magnetic field from 0 to 2 T, 0 to 5 T and 0 to 7 T, the isothermal entropy change reaches maximum values of 3.08, 4.23, and 4.81 J/kg K for *H//a*, while it is only 0.08, 0.41, and 0.79 J/kg K for *H//c*, respectively. The maximum value of $-\Delta S$, along the easy axis and in a field of 7 T, is about ∼6.1 times larger than that along the hard orientation. For the parent compound $TbMn_2O_5$, the maximum value of $-\Delta S$ along the easy axis in a field of 7 T is about ∼63 times larger than that along the hard orientation as previously reported in Ref. [7]. The change of $-\Delta S$ of the parent compound $NdMn_2O_5$ as a function of temperature under several external magnetic fields along the *a* and *c* axes is reported in Fig. S7 [27]. In the field change of 7 T, the computed $-\Delta S$ along the easy axis, is about ∼ 3 times larger than that calculated along the hard orientation. Figure 12 shows the entropy changes related to the rotation of the single crystals $TbMn_2O_5$ [Fig. 12(a)], $Nd_{0.8}Tb_{0.2}Mn_2O_5$ [Fig. 12(b)], and $NdMn_2O_5$ [Fig. 12(c)] from the *c* to *a* direction by 90 ° in different constant magnetic fields initially parallel to the *c* axis. This rotating entropy change can be expressed as follows [7,8,43]: $\Delta S_{R,ca} = \Delta S(H//a) - \Delta S(H//c)$, where $\Delta S(H//a)$ and $\Delta S(H//c)$ are the entropy changes when the magnetic field is applied along the *a* and *c* axes, respectively. Under a magnetic field change of 0–7 T, the temperature corresponding to the maximum of $-\Delta S_R$ is shifted from ∼6 K for $NdMn_2O_5$, to ∼12 K for $Nd_{0.8}Tb_{0.2}Mn_2O_5$, and to ∼15 K for $TbMn_2O_5$.

The refrigerant capacity (RC) is a parameter that has been suggested by Gschneidner and Pecharsky [44] as an important figure of merit for the evaluation of magnetocaloric materials. The RC measures the amount of thermal energy that can be transferred between the hot (T_H) and cold (T_C) reservoirs in one ideal refrigeration cycle. It is defined as

$$\mathrm{RC} = \int_{T_c}^{T_H} \Delta S(T) dT, \tag{16}$$

where T_H and T_C are the temperatures marking the width at half maximum of the $-\Delta S(T)$ profile. The relative cooling power (RCP), which strongly depends on the maximum entropy change ($\Delta S_M^{\max}$) and the FWHM of ΔS peak (δT_{FWHM}) is also usually used to rapidly assess magnetocaloric materials. It is defined as

$$\mathrm{RCP} = \Delta S_M^{\max} \delta T_{\mathrm{FWHM.}} \tag{17}$$

The RC and RCP values as a function of applied magnetic field for $Nd_{0.8}Tb_{0.2}Mn_2O_5$ are presented in Figs. 13(a) and 13(b), respectively. The RC and RCP values presented in filled black circles are directly calculated from the ΔS_R

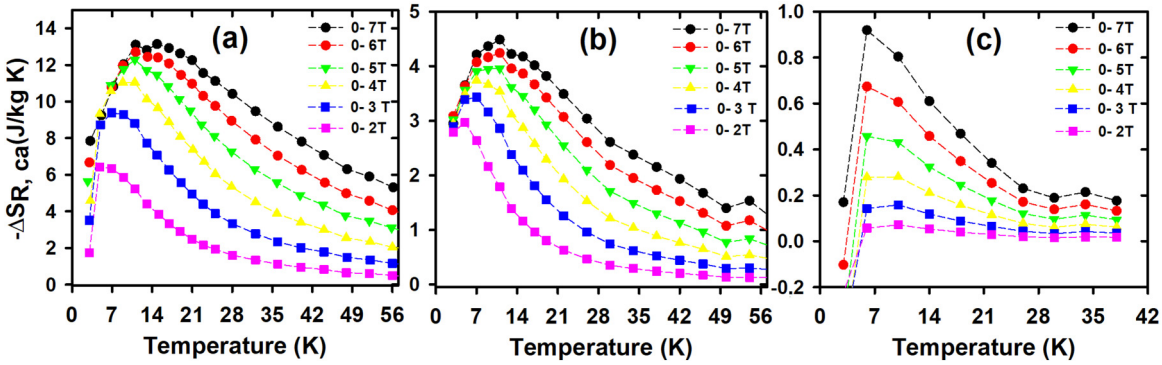

FIG. 12. Entropy changes related to the rotation of the single crystals $TbMn_2O_5$ (a), $Nd_{0.8}Tb_{0.2}Mn_2O_5$ (b), and $NdMn_2O_5$ (c) from the *c* to the *a* direction by 90 ° in different constant magnetic fields, with magnetic field initially parallel to the *c* axis.

change of $Nd_{0.8}Tb_{0.2}Mn_2O_5$. With increasing field, the RC (RCP) increases almost linearly with a rate of about 16 J/kg T (22 J/kg T). Under a magnetic field change of 0–7 T, the RC (RCP) of $Nd_{0.8}Tb_{0.2}Mn_2O_5$ reaches 120 J/kg (144 J/kg), being much larger than that of $NdMn_2O_5$, which is 9 J/kg (11 J/kg), and much smaller than that of $TbMn_2O_5$, which attains 443 J/kg (571 J/kg). As mentioned above, $Nd_{0.8}Tb_{0.2}Mn_2O_5$ presents a magnetic phase separation without a twinning effect. One of them bears the features of $TbMn_2O_5$ and the other one of $NdMn_2O_5$. This implies that the magnetocaloric power of $Nd_{0.8}Tb_{0.2}Mn_2O_5$ could be a result from the contribution of two magnetic phases. To check if the MCE of $Nd_{0.8}Tb_{0.2}Mn_2O_5$ is related to the subtle balance of coexisting magnetic phases, the RC and RCP changes as a function of magnetic field of $Nd_{0.8}Tb_{0.2}Mn_2O_5$ are compared to those of $NdMn_2O_5$ and $TbMn_2O_5$ reference materials. Here, we presume that the fractions of coexisting magnetic phases correspond to the stoichiometric ratios x_{Nd} and x_{Tb} since the Nd phase and Tb phase are induced and stabilized locally by the *R*-ions' anisotropic sites. This means that the RC (RCP) changes of $Nd_{0.8}Tb_{0.2}Mn_2O_5$ can be calculated using a multiple linear analysis of the RC (RCP) values of reference compounds $NdMn_2O_5$ and $TbMn_2O_5$. In this case,

$$RC_{Nd0.8Tb0.2Mn2O5} = x_{Nd}\, RC_{NdMn2O5} + x_{Tb} RC_{TbMn2O5}, \quad (18)$$

$$RCP_{Nd0.8Tb0.2Mn2O5} = x_{Nd} RCP_{NdMn2O5} + x_{Tb} RCP_{TbMn2O5}, \quad (19)$$

where the fitting parameters x_{Nd} and x_{Tb} are 0.8 and 0.2, respectively. Hereafter, RC′ (RCP′) denotes the RC (RCP) of $Nd_{0.8}Tb_{0.2}Mn_2O_5$ deduced from the reference compounds $NdMn_2O_5$ and $TbMn_2O_5$. RC′ and RCP′ are presented in filled red triangles in Figs. 13(a) and 13(b), respectively. Both, RC (RCP) and RC′ (RCP′) present a linear behavior versus magnetic field, with quite a similar rate of about 16 J/kg T (22 J/kg T). This suggests that each Nd- and Tb- separated magnetic phase contributed independently to the magnetocaloric effect of $Nd_{0.8}Tb_{0.2}Mn_2O_5$. However, RC (RCP) is larger and quasiuniformly scaled with respect to RC′ (RCP′). This discrepancy is probably induced by the actual magnetic structures of separated magnetic phases in $Nd_{0.8}Tb_{0.2}Mn_2O_5$, which are slightly different from that of $NdMn_2O_5$ and $TbMn_2O_5$ as reported by Zobkalo *et al.* [19]. More interestingly, the temperature corresponding to the maximum of -ΔS in such separated magnetic phase systems can be shifted from 7 K for $NdMn_2O_5$ to 15 K for $TbMn_2O_5$, which

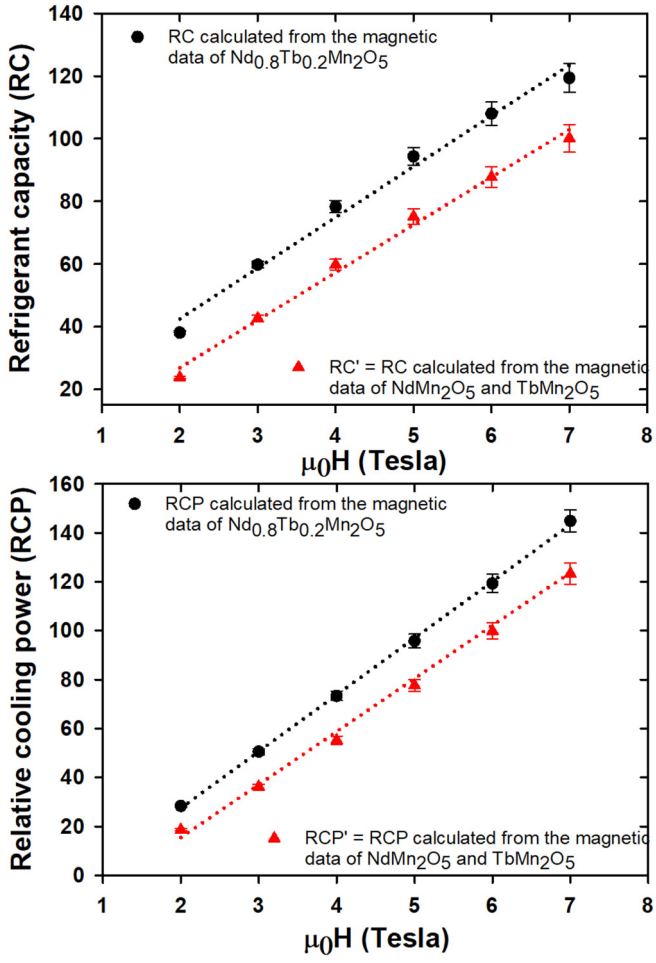

FIG. 13. RC and RCP changes as a function of applied magnetic field for $Nd_{0.8}Tb_{0.2}Mn_2O_5$. The RC and RCP values presented in black circles are directly calculated from the ΔS_R change of $Nd_{0.8}Tb_{0.2}Mn_2O_5$. The RC and RCP values presented in red triangles are calculated from the reference compounds $NdMn_2O_5$ and $TbMn_2O_5$ (RC′ and RCP′).

can control and extend the working temperature range of the magnetocaloric effect. All these findings indicate that for such separated magnetic phase systems, the magnetocaloric effect can be finely tuned by controlling the balance of coexisting magnetic phases.

IV. CONCLUSION

To sum up, the optical and magnetic investigations of the multiferroic and magnetocaloric properties of $Nd_{0.8}Tb_{0.2}Mn_2O_5$ are reported. The Raman phonon frequencies and almost all the CF energy levels of Kramers ion Nd^{3+} and non-Kramers ion Tb^{3+} in $Nd_{0.8}Tb_{0.2}Mn_2O_5$ have been determined and compared to those in the $NdMn_2O_5$ and $TbMn_2O_5$ parent compounds. Raman and infrared data confirm that our $Nd_{0.8}Tb_{0.2}Mn_2O_5$ sample is a single crystal and rule out unequivocally possible twinning. Also, the variation of phonon frequencies and CF excitation energies, with respect to those in $NdMn_2O_5$ and $TbMn_2O_5$, retraces a noticeable change in the Mn1-O3-Mn1 and TbO_8 structural units that could explain the coexistence of separated magnetic phases in $Nd_{0.8}Tb_{0.2}Mn_2O_5$. In addition, we have found that the ground-state Kramers doublet of Nd^{3+} splits into two sublevels below $T_N \sim 30\,\mathrm{K}$, which is associated with the occurrence of Nd phase. This splitting ($\Delta_0 \sim 9\,\mathrm{cm}^{-1}$) is larger than the one reported in $NdMn_2O_5$ ($\Delta_0 \sim 7.5\,\mathrm{cm}^{-1}$), suggesting that the Nd^{3+}–Mn^{3+} interaction is involved in the stability of magnetic and ferroelectric phases in $Nd_{0.8}Tb_{0.2}Mn_2O_5$. The weak Zeeman splitting of excited crystal-field levels of Nd^{3+} under magnetic fields reveals that the g_z factor is weak compared to that in $NdMn_2O_5$. This indicates that the magnetic anisotropy is enhanced and the R^{3+} spins in $Nd_{0.8}Tb_{0.2}Mn_2O_5$ are mostly aligned within the *ab* plane. On the other hand, the magnetocrystalline anisotropy, shown by the whole RMn_2O_5 family, is reviewed and investigated by studying quantitatively the anisotropy of paramagnetic Curie temperatures $\theta_{||} - \theta_{\perp}$ as a function of the rare-earth atomic number. Our theoretical analysis demonstrates that the variation in $\theta_{||} - \theta_{\perp}$ across the rare-earth series is determined by the quadrupolar charge distribution of $4f$ shells, itself determined by the crystal field. The rotating magnetocaloric effect in $Nd_{0.8}Tb_{0.2}Mn_2O_5$ was also evaluated and compared to those of $NdMn_2O_5$ and $TbMn_2O_5$. The result shows that Nd- and Tb-separated magnetic phases contribute independently to the magnetocaloric effect of $Nd_{0.8}Tb_{0.2}Mn_2O_5$.

ACKNOWLEDGMENTS

We acknowledge the technical support of C. Chabanier, S. Pelletier, and J. Rousseau. S.M., S.J., and M.C. would like to thank the Canada Research Chair Program and the Natural Sciences and Engineering Research Council of Canada for their financial support. I.A.Z. is grateful to the Russian Foundation for Basic Research for the financial support (Grant No. 16-02-00545-a). M.B. appreciates the financial support from the International University of Rabat.

[1] N. Hur, S. Park, P. Sharma, J. Ahn, S. Guha, and S-W. Cheong, Nature (London) **429**, 392 (2004).
[2] T. Kimura, T. Goto, H. Shintani, K. Ishizaka, T. Arima, and Y. Tokura, Nature (London) **426**, 55 (2003).
[3] S.-W. Cheong and M. Mostovoy, Nature (London) **6**, 13 (2007).
[4] J. A. Mundy, C. M. Brooks, M. E. Holtz, J. A. Moyer, H. Das, A. F. Rébola, J. T. Heron, J. D. Clarkson, S. M. Disseler, Z. Liu, A. Farhan, R. Held, R. Hovden, E. Padgett, Q. Mao, H. Paik, R. Misra, L. F. Kourkoutis, E. Arenholz, A. Scholl, J. A. Borchers, W. D. Ratcliff, R. Ramesh, C. J. Fennie, P. Schiffer, D. A. Muller, and D. G. Schlom, Nature (London) **537**, 523 (2016).
[5] M. Bibes and A. Barthelemy, Nat. Mater. **7**, 425 (2008).
[6] M. J. Pitcher *et al.*, Science **347**, 420 (2015).
[7] M. Balli, S. Jandl, P. Fournier, and D. Z. Dimitrov, Appl. Phys. Lett. **108**, 102401 (2016).
[8] M. Balli, S. Jandl, P. Fournier, and M. M. Gospodinov, Appl. Phys. Lett. **104**, 232402 (2014).
[9] M. Balli, P. Fournier, S. Jandl, S. Mansouri, A. Mukhin, Y. V. Ivanov, and A. M. Balbashov, Phys. Rev. B **96**, 146401 (2017).
[10] N. Lee, C. Vecchini, Y. J. Choi, L. C. Chapon, A. Bombardi, P. G. Radaelli, and S. W. Cheong, Phys. Rev. Lett. **110**, 137203 (2013).
[11] M. Fukunaga and Y. Noda, J. Phys. Soc. Jpn. **79**, 054705 (2010).
[12] W. Peng, V. Balédent, S. Chattopadhyay, M.-B. Lepetit, G. Yahia, C. V. Colin, M. J. Gooch, C. R. Pasquier, P. Auban-Senzier, M. Greenblatt, and P. Foury-Leylekian, Phys. Rev. B **96**, 054418 (2017).
[13] C. Doubrovsky, G. André, A. Gukasov, P. Auban-Senzier, C. R. Pasquier, E. Elkaim, M. Li, M. Greenblatt, F. Damay, and P. Foury-Leylekian, Phys. Rev. B **86**, 174417 (2012).
[14] S. Chattopadhyay, V. Balédent, F. Damay, A. Gukasov, E. Moshopoulou, P. Auban- Senzier, C. Pasquier, G. André, F. Porcher, E. Elkaim, C. Doubrovsky, M. Greenblatt, and P. Foury-Leylekian, Phys. Rev. B **93**, 104406 (2016); S. Chattopadhyay, V. Baledent, P. Auban-Senzier, C. Pasquier, C. Doubrovsky, M. Greenblatt, and P. Foury-Leylekian, Physica, B **460**, 214 (2015).
[15] S. Mansouri, S. Jandl, M. Balli, P. Fournier, B. Roberge, M. Orlita, I. A. Zobkalo, S. N. Barilo, and S. V. Shiryaev, Phys. Rev. B **98**, 205119 (2018).
[16] I. A. Zobkalo, A. N. Matveeva, A. Sazonov, S. N. Barilo, S. V. Shiryaev, B. Pedersen, and V. Hutanu, Phys. Rev. B **101**, 064425 (2020).
[17] J. A. Alonso, M. T. Casais, M. J. Martinez-Lope, J. L. Martinez, and M. T. Fernandez- Diaz, J. Phys.: Condens. Matter **9**, 8515 (1997).
[18] V. Baledent, S. Chattopadhyay, P. Fertey, M. B. Lepetit, M. Greenblatt, B. Wanklyn, F. O. Saouma, J. I. Jang, and P. Foury-Leylekian, Phys. Rev. Lett. **114**, 117601 (2015); N. Narayanan, P. J. Graham, P. Rovillain, J. O'Brien, J. Bertinshaw, S. Yick, J. Hester, A. Maljuk, D. Souptel, B. Büchner, D. Argyriou, and C. Ulrich, Phys. Rev. B **105**, 214413 (2022).
[19] I. Zobkalo, S. Gavrilov, A. Matveeva, A. Sazonov, S. Barilo, S. Shiryaev, and V. Hutanu, IEEE Trans. Magn. **58**, 1 (2022).

[20] S. Mansouri, S. Jandl, A. Mukhin, V. Y. Ivanov, and A. Balbashov, Sci. Rep. **7**, 13796 (2017).
[21] S. Jandl, S. Mansouri, J. Vermette, A. A. Mukhin, V. Yu Ivanov, A. Balbashov, and M. Orlita, J. Phys.: Condens. Matter **25**, 475403 (2013).
[22] S. Mansouri, S. Jandl, J. Laverdière, P. Fournier, A. A. Mukhin, V. Yu Ivanov, and A. M. Balbashov, J. Phys.: Condens. Matter **25**, 066003 (2013).
[23] S. Mansouri, S. Jandl, B. Roberge, M. Balli, D. Z. Dimitrov, M. Orlita, and C. Faugeras, J. Phys.: Condens. Matter **28**, 055901 (2016).
[24] S. Mansouri, S. Jandl, M. Balli, J. Laverdiere, P. Fournier, and D. Z. Dimitrov, Phys. Rev. B **94**, 115109 (2016).
[25] S. Mansouri, S. Jandl, M. Balli, P. Fournier, Y. Ishii, H. Kimura, M. Orlita, and M. Chaker, Phys. Rev. B **100**, 085147 (2019).
[26] S. Mansouri, S. Jandl, M. Balli, P. Fournier A.A. Mukhin, V. Yu Ivanov, A. Balbashov, and M. Orlita, J. Phys.: Condens. Matter **30**, 175602 (2018).
[27] See Supplemental Material at http://link.aps.org/supplemental/10.1103/PhysRevB.106.085107 for additional figures.
[28] B. Mihailova, M. M. Gospodinov, B. Güttler, F. Yen, A. P. Litvinchuk, and M. N. Iliev, Phys. Rev. B **71**, 172301 (2005).
[29] A. P. Litvinchuk, J. Magn. Magn. Mater. **321**, 2373 (2009).
[30] T. A. Tyson, M. Deleon, S. Yoong, and S-W. Cheong, Phys. Rev. B **75**, 174413 (2007).
[31] L. F. Chibotaru, A. Ceulemans, and H. Bolvin, Phys. Rev. Lett. **101**, 033003 (2008).
[32] J. Hemberger, M. Brando, R. Wehn, V. Yu. Ivanov, A. A. Mukhin, A. M. Balbashov, and A. Loidl, Phys. Rev. B **69**, 064418 (2004).
[33] M. H. Phan, M. B. Morales, N. S. Bingham, H. Srikanth, C. L. Zhang, and S. W. Cheong, Phys. Rev. B **81**, 094413 (2010).
[34] N. Hur, S. Park, P. A. Sharma, S. Guha, and S.-W. Cheong, Phys. Rev. Lett. **93**, 107207 (2004).
[35] A. M. Kadomtseva, S. S. Krotov, Y. F. Popov, G. P. Vorobev, and M. M. Lukina, JETP **100**, 305 (2005).
[36] M. Uga, N. Iwata, and K. Kohn, Ferroelectrics **219**, 55 (1998).
[37] Y. Koyata, H. Nakamura, N. Iwata, A. Inomata, and K. Kohn, J. Phys. Soc. Jpn. **65**, 1383 (1996).
[38] B. Kh. Khannanov, V. A. Sanina, E. I. Golovenchits, and M. P. Scheglov, J. Magn. Magn. Mater. **421**, 326 (2017).
[39] V. A. Sanina, B. Kh Khannanov, and E. I. Golovenchits, Phys. Solid State **59.10**, 1952 (2017).
[40] G. R. Blake, L. C. Chapon, P. G. Radaelli, S. Park, N. Hur, S.-W. Cheong, and J. Rodríguez-Carvajal, Phys. Rev. B **71**, 214402 (2005).
[41] V. Skumryev, M. D. Kuz'min, M. Gospodinov, and J. Fontcuberta, J. Phys. Rev. B **79**, 212414 (2009).
[42] M. D. Kuz'min and A. M. Tishin, in *Handbook of Magnetic Materials*, edited by K. H. J. Buschow (North-Holland, Amsterdam, 2008), Vol. 17, p. 159.
[43] M. Balli, S. Jandl, P. Fournier, and A. Kedous-Lebouc, Appl. Phys. Rev. **4**, 021305 (2017).
[44] K. A. Gschneidner Jr. and V. K. Pecharsky, Annu. Rev. Mater. Sci. **30**, 387 (2000).